STRUCTURAL BIOLOGY

Structure of S1PR2–heterotrimeric G_{13} signaling complex

Hongwen Chen[1], Kevin Chen[2], Weijiao Huang[1], Louis M. Staudt[3], Jason G. Cyster[2,4]*, Xiaochun Li[1,5]*

Sphingosine-1-phosphate (S1P) regulates immune cell trafficking, angiogenesis, and vascular function via its five receptors. Inherited mutations in S1P receptor 2 (S1PR2) occur in individuals with hearing loss, and acquired mutations in S1PR2 and $G_{\alpha 13}$ occur in a malignant lymphoma. Here, we present the cryo–electron microscopy structure of S1P-bound S1PR2 coupled to the heterotrimeric G_{13}. Interaction between S1PR2 intracellular loop 2 (ICL2) and transmembrane helix 4 confines ICL2 to engage the $\alpha 5$ helix of $G_{\alpha 13}$. Transforming growth factor–α shedding assays and cell migration assays support the key roles of the residues in S1PR2-$G_{\alpha 13}$ complex assembly. The structure illuminates the mechanism of receptor disruption by disease-associated mutations. Unexpectedly, we showed that FTY720-P, an agonist of the other four S1PRs, can trigger G_{13} activation via S1PR2. S1PR2^{F274I} variant can increase the activity of G_{13} considerably with FTY720-P and S1P, thus revealing a basis for S1PR drug selectivity.

INTRODUCTION

The diversity of lipids ensures the structural rigidity and flexibility of cellular membranes. Lipids and their metabolites also serve as extracellular ligands for more than 50 G protein (heterotrimeric guanine nucleotide–binding protein)–coupled receptors (GPCRs), enabling the transduction of signals from the cell surface into the intracellular space (*1–3*). Sphingosine-1-phosphate (S1P), a signaling sphingolipid, functions as a regulator of the human immune and vascular systems through binding G protein–coupled S1P receptors (S1PR1 to S1PR5) (fig. S1) (*4–7*). S1P can act to increase or decrease vascular permeability, cell growth, and cell migration depending on which receptor is engaged, and it plays a crucial role in promoting lymphocyte egress from lymphoid organs by engaging S1PR1. Several S1PRs modulators—including Fingolimod (FTY720), Siponimod, and Ozanimod—have been approved for treating the autoimmune disease multiple sclerosis (*8–10*).

Intriguingly, the five S1PRs share high sequence homology but have been shown to bind different G proteins (*11*, *12*). G proteins are classified into four families according to their α subunit: G_i, G_s, $G_{q/11}$, and $G_{12/13}$. S1PR1 and S1PR5 couple preferentially to $G_{i/o}$, while S1PR2 and S1PR3 can couple to $G_{i/o}$, $G_{q/11}$, and $G_{12/13}$ (*11–13*). In the case of S1PR2, in vivo studies in lymphocytes have shown a strict dependence on $G_{\alpha 13}$ (*14*, *15*), and endothelial S1PR2 also appears to signal dominantly via $G_{\alpha 12}$ or $G_{\alpha 13}$ (*16*). Inherited missense mutations in S1PR2 have been identified in patients with hearing impairment, and mice lacking S1PR2 are deaf due to functional defects in auditory and vestibular systems (*17*, *18*). Acquired mutations in GNA13 (encoding $G_{\alpha 13}$) and S1PR2 were found in germinal center B cell–like diffuse large B cell lymphoma (GCB-DLBCL) by deep sequencing studies (*15*, *19–21*). Deficiency in S1PR2 or $G_{\alpha 13}$ caused a loss of germinal center B cell confinement and was sufficient to cause lymphomagenesis (*14*, *15*), demonstrating the important role of $G_{\alpha 13}$ in inhibiting the growth and dissemination of germinal center B cells (*15*).

Previous structural studies on S1PRs have provided important insights into receptor-ligand interactions and G protein coupling. The crystal structure of S1PR1 bound to the sphingosine-mimic antagonist ML056 presented the inactive state of S1PRs (*22*), and comparison to the crystal structure of S1P-bound S1PR3 revealed transmembrane-domain residues that may regulate G protein selectivity (*23*). Recently, the structures of S1PR1, S1PR3, and S1PR5 coupled to G_i in the presence of different agonists provided a molecular basis for S1PR-mediated G_i activation (*24*, *25*). However, the molecular details of how S1PRs recruit heterotrimeric G_{13} protein remain unknown. Notably, G_{13} plays an important role in regulating cell migration and actin cytoskeletal remodeling (*26*), and there is no available structure of any GPCR coupled to $G_{12/13}$ to date. Because $G_{\alpha 12}$ and $G_{\alpha 13}$ share high sequence homology and, sometimes, function redundantly in signal transmission (*26*), structural studies on the S1PR2-G_{13} complex will provide molecular insights into the $G_{12/13}$ activation mechanism that may apply to other GPCRs, as well as the molecular basis for $G_{12/13}$ protein coupling.

RESULTS

Structure of S1PR2-G_{13} complex

We purified human S1PR2 in the presence of S1P and incubated with $G_{\alpha 13\beta 1\gamma 2}$ heterotrimer. However, the complex was unstable in solution during purification. We then substituted the αN helix of wild-type $G_{\alpha 13}$ with the αN helix of $G_{\alpha i}$ (referred here as "G_{13iN}") according to previous studies (*27*, *28*). To stabilize the complex, we added scFv16, which binds to G_{13iN}-αN and G_β (*29*). The purified complex was concentrated for cryo–electron microscopy (cryo-EM) studies (fig. S2A). We obtained 13 million particles from ~33,000 cryo-EM images. The particles exhibit severe dissociation upon grid preparation, resulting in only 5% of the particles in complex for final three-dimensional (3D) reconstruction (fig. S2B and table S1). The

[1]Department of Molecular Genetics, University of Texas Southwestern Medical Center, Dallas, TX 75390, USA. [2]Department of Microbiology and Immunology, University of California, San Francisco, San Francisco, CA 94143, USA. [3]Lymphoid Malignancies Branch, Center for Cancer Research, National Cancer Institute, National Institutes of Health, Bethesda, MD 20892, USA. [4]Howard Hughes Medical Institute, University of California, San Francisco, San Francisco, CA 94143, USA. [5]Department of Biophysics, University of Texas Southwestern Medical Center, Dallas, TX 75390, USA.
*Corresponding author. Email: jason.cyster@ucsf.edu (J.G.C.); xiaochun.li@utsouthwestern.edu (X.L.)

overall structure was determined at 3.2 Å resolution by 640,483 particles. The structure revealed well-defined features for the canonical seven transmembrane helices (7-TMs) of S1PR2, the G_{13iN} Ras-like domain, the G_β and G_γ subunits, and scFv16 (Fig. 1A and figs. S2, C and D, and S3). The density of the S1P ligand was observed in the cavity created by the transmembrane region (Fig. 1B).

The TMs generate an amphiphilic pocket with a positively charged head in the outer leaflet and hydrophobic region in the middle of the receptor to accommodate the S1P ligand (Fig. 1B). Several polar residues are responsible for binding the sphingosine head and phosphate group, and several hydrophobic residues contact the alkyl tail of S1P (Fig. 1C). The N-terminal helix (NTH) functions as a lid to retain the ligand in the cavity (Fig. 1C). We used the established transforming growth factor–α (TGF-α) shedding assay that reports on heterotrimeric G protein signaling to validate S1P-mediated S1PR2 coupling (11, 30). The human S1PR2 (wild-type or point mutant variants), $G_{\alpha q/13}$ (a chimeric G_q with $G_{\alpha 13}$-α5 helix), and alkaline phosphatase–fused TGF-α (AP–TGF-α) were cotransfected

into human embryonic kidney (HEK) 293 $\Delta G_{q/11/12/13}$ cells to measure G protein signal. We obtained a potency [median effective concentration (EC$_{50}$)] and an amplitude of ligand-induced response (E_{max}) from the sigmoidal concentration-response curve of each variant. The results show that S1P can activate S1PR2 and trigger $G_{\alpha q/13}$ protein signaling (fig. S4A). Mutations on the key residues that accommodate the sphingosine head (Y18^{NTH}, N89$^{2.60}$, R108$^{3.28}$, and E109$^{3.29}$, superscripts refer to Ballesteros-Weinstein number) interfere with the EC$_{50}$ and/or E_{max} of S1P activity considerably (Fig. 1, C to E, and fig. S4A), while mutations on the residues that contact the alkyl tail (F113$^{3.33}$ and L116$^{3.36}$) attenuate the E_{max} of S1PR2 (Fig. 1E and fig. S4A).

Structural comparisons reveal activation mechanism

Comparison of our G_{13} structure with a guanosine diphosphate (GDP)–bound G_{13} structure provides molecular insights into the structural rearrangements associated with S1PR2-induced G_{13} activation (28). The $G_{\alpha 13}$-α5 undergoes a notable conformational change
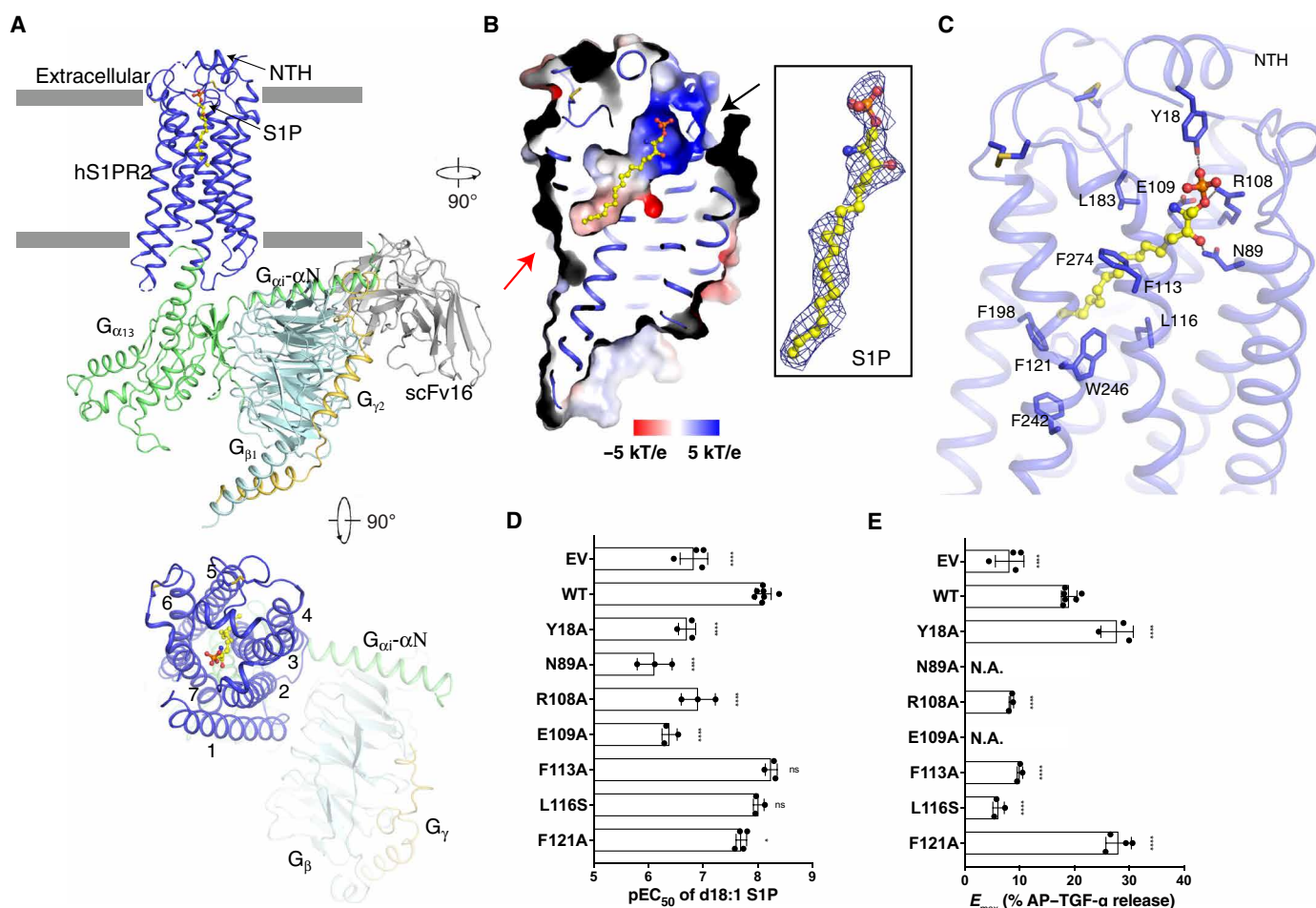

Fig. 1. Overall structure of S1PR2-G$_{13}$ complex and the S1P binding site. (**A**) Ribbon representation of the structure viewed from the side of the membrane (top) and the extracellular space (bottom). NTH, N-terminal helix. (**B**) Electrostatic surface representation of S1PR2 and the cryo-EM map of d18:1 S1P ligand (yellow sticks) at 5σ level. The putative S1P entrances are indicated by black arrow (the outer leaflet) and red arrow (the lipid bilayer). (**C**) Interaction details of S1P with residues in the binding site indicated. (**D** and **E**) Comparison of pEC$_{50}$ values and E_{max} of each variant. The representative dose-response curves from same-day experiment and membrane expression of S1PRs are shown in fig. S4A. The not applicable (N.A.) value means curve not reaching E_{max}. Data are means ± SD ($n = 3$ to 7 independent experiments). *$P < 0.05$ and ****$P < 0.0001$, mutant versus wild-type (WT) values according to one-way analysis of variance (ANOVA) with Dunnett's multiple comparison test. ns, not significant. AP–TGF-α, alkaline phosphatase–fused TGF-α. EV, empty vector.

with a translation of more than 6 Å and a ~45° rotation upon nucleotide release (Fig. 2A). The conformational change of α5 accompanies the concerted movements of the β6-α5 loop and the α1 helix (Fig. 2A). This reorganization is consistent with the findings in other GPCR-engaged G_i, G_s, and G_q proteins (27, 31, 32). The shift of the α5 induces a movement of the β6-α5 loop of more than 5 Å. This movement enhances the hydrogen bond between Q67 and the backbone carbonyl of N351 and relieves the interactions between

the β6-α5 loop and the guanine base of GDP to further trigger GDP dissociation from G_{13} (Fig. 2A). The nucleotide-free G_{13} protein may, in turn, allosterically enhance S1P-binding affinity as suggested by studies on the β2-adrenergic receptor (33).

Structural comparison of our active S1PR2 structure with the inactive S1PR1 state (22) suggests that S1P induces the conformational changes of several hydrophobic residues, including $F113^{3.33}$, $F121^{3.41}$, $F198^{5.47}$, and $W246^{6.48}$ in the center of S1PR2 (Fig. 2B and fig. S5A).
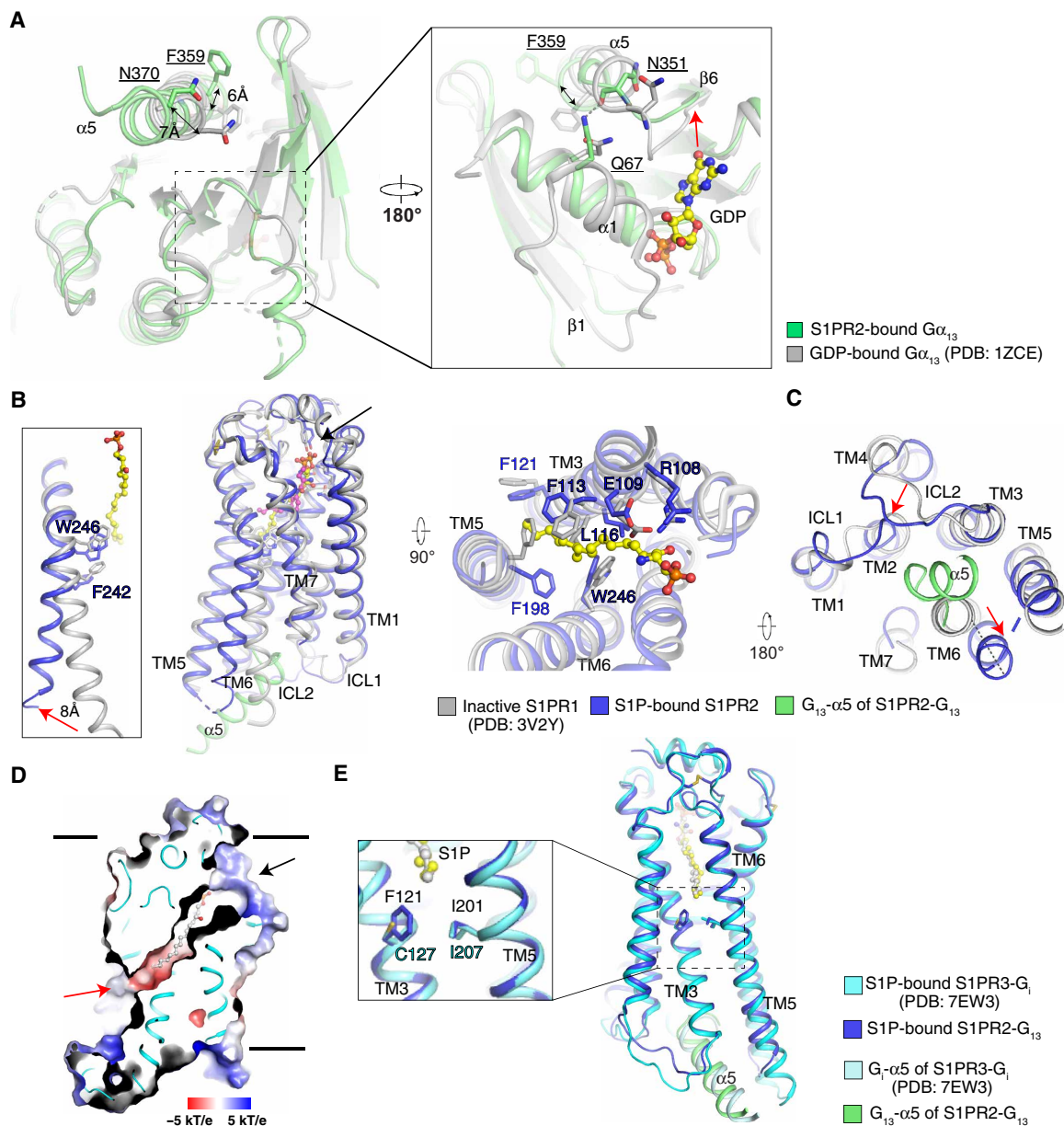

Fig. 2. Structural comparisons reveal conformational changes associated with activation and differences in ligand access. (**A**) Structural comparison with GDP-bound $G_{\alpha13}$ with S1PR2-coupled $G_{\alpha13}$. The movement of β6-α5 loop is indicated by a red arrow. (**B**) Superimposition of TMs of inactive S1PR1- and S1P-bound S1PR2 viewed from the side of the membrane (left) and extracellular space (right). The antagonist ML056 of S1PR1 is shown as magenta sticks, and the S1P is shown as yellow sticks. The residues that engage the ligands are shown in sticks. The movements of TM6 in the G_{13}-bound S1PR2 compared with the inactive S1PR1 are shown with red arrow. The putative S1P entrance in the outer leaflet is indicated by black arrow. (**C**) Superimposition as in (B) but viewed from the side of the cytosol. The movements of TMs are indicated by red arrows. (**D**) Electrostatic surface representation of S1PR3. The putative S1P entrances are indicated by black arrow (the outer leaflet) and red arrow (the lipid bilayer). The S1P is shown as gray sticks. (**E**) Superimposition of TMs of S1P-bound S1PR2 and S1PR3 viewed from the side of the membrane. The comparison of the putative S1P entrance is zoomed.

The shift of W246[6.48] further forces F242[6.44] toward the edge of the receptor to trigger the notable movement of TM6 that is characteristic of receptor activation (Fig. 2B) (*34*). This conformational change creates enough room in the cytosolic side of S1PR2 to accommodate the $G_{\alpha 13}$-$\alpha 5$ (Fig. 2C). The structural analysis reveals that the alkyl tail of S1P stimulates the movement of the PIF motif (fig. S5B), and Y209[5.58] and Y288[7.53] of the NPXXY motif have a hydrophilic interaction in the active S1PR2 (fig. S5, C and D), resembling the activation of other class A GPCRs (*34, 35*).

The smoothened (SMO) receptor structures showed a cholesterol entrance in the middle of its transmembrane domain (*36, 37*), suggesting that lipid substrates may access the receptor from deep within the lipid bilayer. In contrast, the structures of S1PR1 and S1PR3 showed that a cavity opens to the outer leaflet, suggesting an entrance of S1P between TM1 and TM7 close to the membrane surface (Fig. 2, B and D) (*22, 23, 38*). The S1P-bound S1PR3 also revealed an opening to the middle of the lipid bilayer, implying that S1P may access the receptor through a deep bilayer entrance (Fig. 2D) (*23*); however, the analogous cavity is closed in S1PR2 (Fig. 1B). F121[3.41] of S1PR2, which provides hydrophobic contacts with the alkyl tail of S1P, may impede the access of S1P via the 7-TMs deep within the bilayer (Fig. 2E). The TGF-α shedding assay shows that the F121A mutation leads to a slight decrease of the EC_{50} of S1P but considerably enhances the E_{max}, which implies that reducing the steric hindrance of the putative lipid entrance via the 7-TMs deep in the bilayer may accelerate the access of S1P into the receptor (Fig. 1, D and F, and fig. S4A). S1P may enter via the membrane, perhaps after delivery by one of the two best defined carriers (e.g., apolipoprotein M+ high-density lipoprotein and albumin (*39*)].

The receptor and $G_{\alpha 13}$ interface

In the active conformation, E129[3.49] of the DRY motif forms an intramolecular bond with Y140[ICL2] and a salt bridge with R147[4.41] (Fig. 3, A and B). These interactions likely stabilize $G_{\alpha 13}$-N370 through a hydrophilic bond between N370 and the main chain amino group of Y140[ICL2], keeping V137[ICL2] and L139[ICL2] buried in the hydrophobic groove generated by the $\beta 1$, $\beta 3$, $\beta 2$-$\beta 3$ loop, and $\alpha 5$ of $G_{\alpha 13}$ (Fig. 3, B and C). Our previous work showed that mutant R147C loses germinal center growth suppressive activity (*15*), thus providing physiological evidence to support our observation. This finding is also supported by a previous study that demonstrated that the intracellular loop 2 (ICL2) plays a key role in the G protein selectivity (*40*). The Q373 of $G_{\alpha 13}$-$\alpha 5$ binds S66[2.37] through hydrophilic interactions to confine the ICL1 (Fig. 3C). Moreover, L371, L374, M375, and Q377 contact M68[2.39], L72[2.43], R130[3.50], I134[3.54], V216[5.65], T228[6.30], and L232[6.34], thus building the interaction network between $G_{\alpha 13}$ and S1PR2 (Fig. 3D).

The intramolecular interaction between the E129[3.49] of the DRY motif and Y140[ICL2] in S1PR2 facilitates the coupling of the receptor to $G_{\alpha 13}$-$\alpha 5$; however, the conserved tyrosine in the S1PR3-G_i complex did not bind to E135[3.49] of the DRY motif (Fig. 3E) (*25*). Instead, it interacts with the T219 of $G_{\alpha i}$ to aid the interactions between receptor and $G_{\alpha i}$. While superimposing the S1PR3-G_i complex onto the S1PR2-G_{13} complex, the Y146[ICL2] of S1PR3 would be predicted to clash with the $\beta 1$ of G_{13} (Fig. 3E). However, our study along with prevous studies (*11–13*) showed that S1PR3 is also able to engage G_{13} (fig. S6A). Because Y140[ICL2] is only conserved between S1PR2 and S1PR3 (fig. S1), it is tempting to speculate that the conserved tyrosine in S1PR3 may adopt a similar conformation as that in the S1PR2-G_{13} complex when S1PR3 couples to G_{13}.

Although the overall arrangement of S1PR2-G_{13} is similar to other GPCR–G protein complexes (including M1-G_q, μR-G_i, and $\beta 1$-G_s complexes) (*27, 31, 41*), several distinct features are apparent (figs. S7 and S8). Superimposing the structure of S1PR2 with M1 in its G_q-bound complex shows a different orientation of the G protein relative to the receptor (fig. S7A). The C terminus of M1 inserts into the cavity between G_α and G_β, but the C-terminal tail of S1PR2 is not resolved in the cryo-EM map (fig. S7B). The ICL2 of M1, μR-G_i, and $\beta 1$ forms a helix, while ICL2 of S1PR2 resembles a loop and faces inward toward the $\alpha 5$ (figs. S7C and S8, A and B). The extensive contacts between the ICL2 of S1PR2 and $G_{\alpha 13}$-$\alpha 5$ induce a ~10° rotation of $\alpha 5$ toward TM5 and TM6, which is more than in the other complexes (figs. S7C and S8, A and B). In S1PR2-G_{13} and M1-G_q complexes, the Gln residue in $\alpha 1$ has a hydrophilic interaction with the $\beta 6$-$\alpha 5$ loop to assist the disassociation of the nucleotide and retain the conformation of $\alpha 5$ for recruiting the receptor (fig. S7D). The structures of the active aminergic receptors reveal that the conserved Tyr in ICL2 also forms a hydrogen bond with Asp[3.49] of the DRY motif (Fig. 3F) (*32, 41*). The ICL2 of the $\beta 1$ receptor does not contact with G_s-$\alpha 5$; in contrast, the flexibility of S1PR2-ICL2 allows Y140[ICL2] to form the hydrogen bond with N370 of $G_{\alpha 13}$-$\alpha 5$ (Fig. 3B). Furthermore, unlike R147[4.41] of S1PR2, which forms a hydrophilic network with E129[3.49] and Y140[ICL2] (Fig. 3B), R155[4.41] of the $\beta 1$ receptor binds the backbone carbonyl of T74[ICL1], thus keeping ICL2 away from G_s-$\alpha 5$ (Fig. 3F).

To validate this interface, we performed a substantial mutagenesis study using TGF-α shedding assays. The E_{max}/EC_{50} value of each variant was normalized by the value of the wild-type protein to generate a relative intrinsic activity (RAi). Then, LogRAi is ranged from −2 to 0 and used as an indicator of G protein coupling (*11*). Either S1PR2 (S66[2.37], L72[2.43], R130[3.50], I134[3.54], and Y140[ICL2]) or $G_{\alpha 13}$ (N370, L371, and M375) variant presents less intrinsic activity than the wild-type complex (Fig. 4, A and B, and fig. S4, B and C). Although the LogRAi of $G_{\alpha 13}$[Q377A] did not decrease, the mutation affects the E_{max} and EC_{50}, weakening the activation of G protein signaling via S1PR2 (Fig. 4B and fig. S4C).

To further validate the physiological role of the S1PR2-G_{13} complex, we tested four S1PR2 mutations (S1PR2[N89A], S1PR2[R108A], S1PR2[I134A], and S1PR2[Y140A]) for their influence on S1P-mediated migration inhibition of WEHI-231 B lymphoma cells (Fig. 4C and fig. S9). Three of the mutants caused an almost complete loss of S1P-mediated migration inhibition, while the S1PR2[I134A] mutant had only a mild effect, findings in close accord with the TGF-α shedding assay (Fig. 4A). We also tested two G_{13} mutations (G_{13}-N370A and G_{13}-M375A) in the migration inhibition assay by introducing them into the M12 B lymphoma line that expresses S1PR2 but lacks endogenous G_{13} function. Both mutations led to a severe defect in the ability of S1P to mediate migration inhibition (Fig. 4D). These data further support the conclusions from the TGF-α shedding assays regarding the physiological relevance of the structural observations. Thus, our findings reveal the molecular basis of how S1PR2 couples to G_{13} protein.

Unique drug selectivity of S1PR2

Fingolimod/FTY720 is used for multiple sclerosis treatment. FTY720 can be converted to FTY720 (S)-phosphate (FTY720-P) by sphingosine kinase 2 in vivo (*42*), which then stimulates the internalization of S1PR1 on lymphocytes, inhibiting their migration to S1P and egress from lymphoid tissues (*43, 44*). Previous studies showed that FTY720-P also binds and activates S1PR3, S1PR4, and S1PR5 (*44, 45*). In particular,
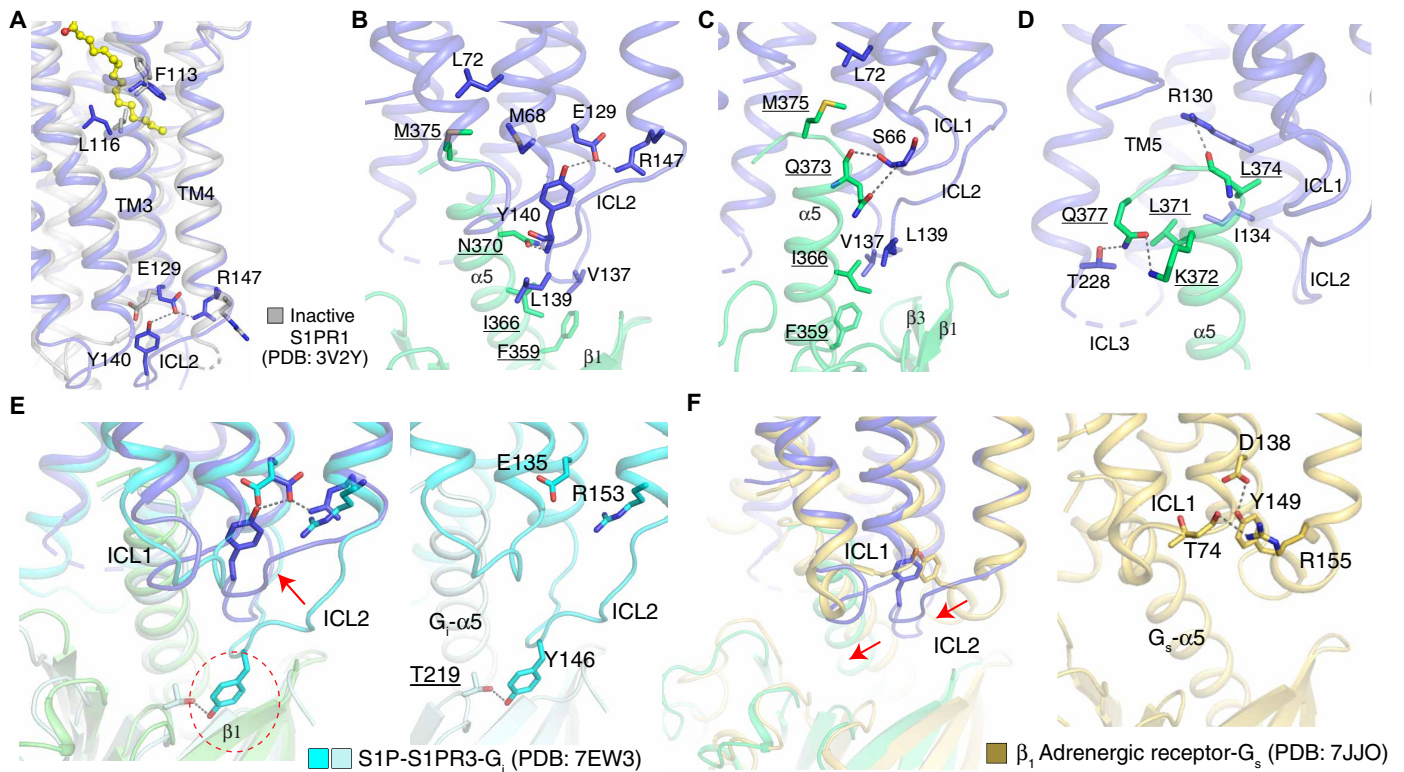
Fig. 3. Interaction details between S1PR2 and $G_{\alpha13}$. (**A**) The structural comparison of the inactive S1PR1 (gray) with S1PR2. (**B** to **D**) The interactions between S1PR2 (blue) and $G_{\alpha13}$ (green). The hydrophilic interaction is indicated by the dashed line, and the residues of $G_{\alpha13}$ are underlined. (**E**) Comparison of ICL2 in S1PR2-G_{13} complex and S1PR3-G_i complex. The putative steric clash between Y145 of S1PR3 and β1 of G_{13} is indicated by a red dashed circle. The interaction detail between S1PR3 and G_i is shown on the right. (**F**) Comparison of ICL2 in S1PR2-G_{13} complex and β1-G_s complex. The interaction detail between β1 and G_s is shown on the right. The interactions between the residues are indicated by dashed lines. The structural differences between the receptors are indicated by arrows.

FTY720-P acts as a biased agonist to trigger G_i and $G_{12/13}$ signaling (Fig. 5A) but not G_q signaling via S1PR3, causing off-target effects (23, 46). Early studies indicated that FTY720-P did not engage S1PR2 (44, 45), and this is still a widely held view (5, 6), although cell signaling studies have suggested that S1PR2 can be activated by FTY720-P for coupling $G_{12/13}$ (47) and β-arrestin (48). Thus, there is still some uncertainty in the possible effect of FTY720-P on S1PR2.

Our TGF-α shedding assays show that FTY720-P, like S1P, can trigger strong $G_{q/13}$ activation via S1PR2 (Fig. 5A and fig. S6A). The shedding assays also reveal that S1P and FTY720-P can weakly activate $G_{q/i}$ via S1PR2, although only near the micromolar range (Fig. 5A and fig. S6, A and B). In contrast, FTY720-P and S1P can trigger the activation of both $G_{q/i}$ and $G_{q/13}$ via S1PR3 equally (fig. S6, A to D). Notably, the FTY720-P–mediated S1PR2 activation can be abolished by the highly S1PR2 selective inhibitor JTE-013 (49). However, JTE-013 cannot interfere with the FTY720-P–mediated S1PR3 activation, demonstrating that FTY720-P can specifically trigger S1PR2 activation (Fig. 5B). These findings extend the evidence for selective coupling of S1PR2 to $G_{\alpha13}$ versus $G_{\alpha i}$ while also showing that S1PR3 signals via $G_{\alpha13}$ and $G_{\alpha i}$ with similar efficiency (fig. S6D). Dual signaling via $G_{\alpha i}$ and $G_{\alpha12/13}$ has been linked to enhancements in directed cell migration (50) and might contribute to the efficacy of S1PR3 as a promigratory receptor (51, 52). By contrast, the near selective $G_{\alpha13}$ coupling of S1PR2 may be critical for its ability to antagonize S1PR1-mediated $G_{\alpha i}$ responses and thereby promote lymphocyte retention in tissues (53).

To uncover the molecular details of FTY720-P selectivity in S1PRs, we compared the structures of S1PRs. $F274^{7.39}$ of S1PR2 contacts $L253^{6.55}$ to force $F250^{6.52}$ to face the edge of S1PR2 and thereby adopt a unique conformation compared to that of inactive S1PR1 and active S1PR3 (Fig. 5C). Notably, F274 is not conserved in the other S1PRs (fig. S1), but it is widely conserved in S1PR2 across different species, implying that this residue may play a unique role in the ligand recognition of S1PR2 (Fig. 5D). The shedding assay shows that the $S1PR2^{F274I}$ variant presents an increased efficacy for S1P-mediated $G_{q/13}$ activation (Fig. 5, E and F) and stronger potency and efficacy for FTY720-P–mediated $G_{q/13}$ activation (Fig. 5, G and H), because it may reduce the steric hindrance of $F250^{6.52}$ with $L253^{6.55}$ to facilitate ligand engagement and the structural rearrangement of TM6. F274I mutation leads to a reduced response of S1PR2 to its inhibitor JTE-013 (Fig. 5B).

As further tests of the ability of FTY720-P to engage S1PR2, we conducted S1PR2 internalization and migration inhibition experiments. Immunofluorescence microscopy of S1PR2-expressing HEK293 cells and flow cytometric anlaysis of S1PR2-expressing WEHI-231 cells showed that FTY720-P caused internalization of S1PR2 with similar efficacy to S1P when used at 1 μM (Fig. 6, A and B). Moreover, FTY720-P was active in inhibiting migration of S1PR2-expressing WEHI-231 cells to CXC motif chemokine ligand 12 (CXCL12) (Fig. 6C). Together, these findings confirm that FTY720-P can act as an agonist of S1PR2, and they show the essential role and unique feature of $S1PR2$-$F274^{7.39}$ in FTY720-P selectivity.
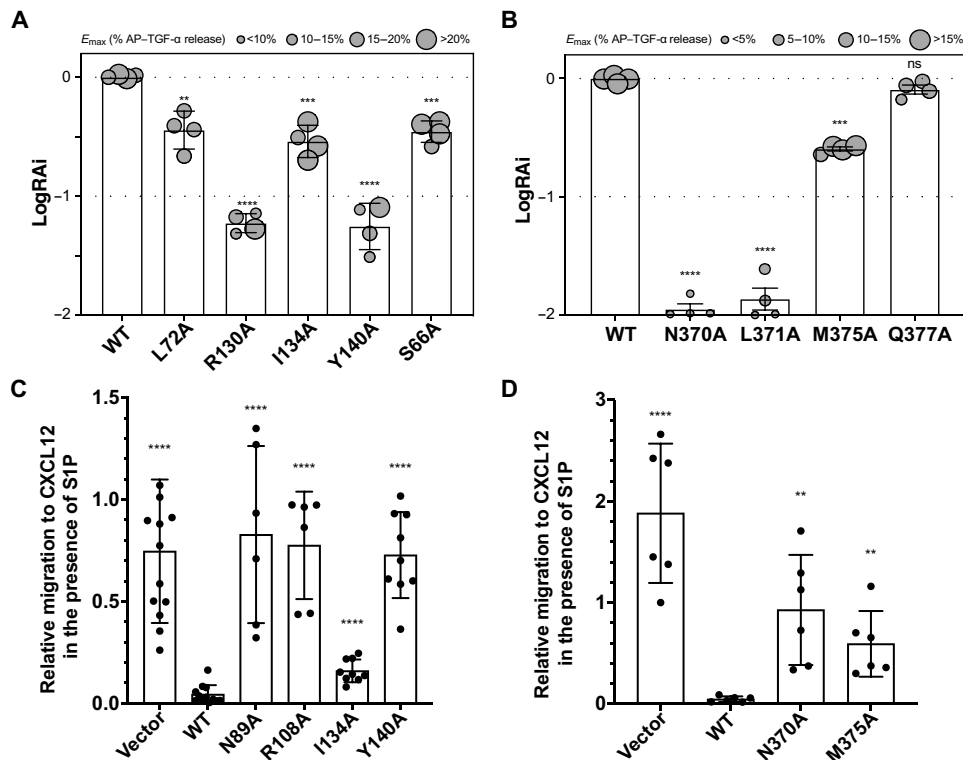
Fig. 4. The physiological importance of S1PR2 and $G_{\alpha 13}$ interface. (**A** and **B**) Relative intrinsic activity (RAi) of each varient of S1PR2 (A) and $G_{\alpha 13}$ (B). G protein coupling is scored as logarithmic values of RAi, which is defined as a relative E_{max}/EC_{50} value normalized by the wild-type value. Symbol size is proportional to E_{max}. Each LogRAi plot denotes a single measurement from a dose-response experiment. The representative dose-response curves from same-day experiment and protein expression are shown in fig. S4 (B and C). Data are means ± SD ($n = 4$ independent experiments). (**C**) Cell migration inhibition assay with S1PR2 wild-type, S1PR2 variant, or control (vector) expressing WEHI-231 cells. Membrane expression of S1PRs is shown in fig. S9. Data are means ± SD (pooled from three to four independent experiments). (**D**) Cell migration inhibition assay with $G_{\alpha 13}$ wild-type, $G_{\alpha 13}$ variant, or control (vector) expressing M12 cells. Data are means ± SD (pooled from three independent experiments). **$P < 0.01$, ***$P < 0.001$, and ****$P < 0.0001$; mutant versus wild-type values according to one-way ANOVA with Dunnett's multiple comparison test.

Disease-associated S1PR2 variants

The physiological importance of the S1PR2-G_{13} complex in lymphoma has been demonstrated (*15*, *54*, *55*). We have mapped a series of GCB-DLBCL–associated mutations (*15*, *19–21*, *56–59*) into the complex structure (fig. S10). Mutations in S1PR2 in either the S1P binding site (including Y18, N89, R108, E109, and L116) or the $G_{\alpha 13}$ interface (including L72, I134, Y140, and R147) cause a substantial reduction in G protein signaling (Figs. 1, D and E, and 4, A and C) (*15*). Moreover, mutations of $G_{\alpha 13}$ on the receptor interface (including N370, L371, M375, and Q377) also attenuate G protein signaling (Fig. 4, B and D). These findings support that GCB-DLBCL–associated mutations, which may not be predicted to disrupt protein expression, are likely to reduce or abolish ligand binding or the S1P-mediated activation of G_{13}, thereby contributing to tumorigenesis.

Three S1PR2 variants have been associated with hearing loss in humans: R108P, R108Q, and Y140C (*17*, *18*). The R108A variant interferes with ligand binding directly, reducing the S1P ligand potency (Fig. 1D). Given that R108 interacts with the phosphate group of S1P, mutation to Pro and Gln would weaken the S1P engagement. A change of Y140 to Cys would have a similar adverse impact on bonding to E129 of the DRY motif as a change to Ala, thereby abolishing interaction with $G_{\alpha 13}$-α5 (Fig. 4, A and C). A mouse S1PR2^{T289R} variant (also T289 in human) was identified as the *stonedeaf*

mutation (*60*). Residue T289 is located in the C terminus of TM7 (fig. S10, A and C) and close to the NPXXY motif. This variant likely interferes with the cytosolic side of the receptor that recruits the $G_{\alpha 13}$-α5 or affects conformational rearrangement of the NPXXY motif for receptor activation. The genetic findings along with our structural analysis suggest the S1PR2-G_{13} signaling complex may contribute to the biogenesis of the auditory system.

DISCUSSION

Here, we report the cryo-EM structure of S1P-bound S1PR2 coupled to heterotrimeric G_{13} protein. The structure adds to the existing evidence that lipid ligands of GPCRs access their binding pockets through an opening within the lipid bilayer. These findings suggest that S1P must partition into the plasma membrane of the S1PR-expressing cell before engaging the receptor. A key distinction from other GPCR structures is the presence of an intramolecular hydrogen bond between the DRY motif and a tyrosine in ICL2 that allows insertion of $G_{\alpha 13}$-α5. Notably, this tyrosine is conserved in S1PR3, the only other S1PR also able to couple G_{13}. This structure explains how multiple S1PR2 and $G_{\alpha 13}$ variants arising in GCB-DLBCL lead to receptor dysfunction and thus deregulated migration and growth of germinal center B cells. It also illuminates the disruptive properties of hearing loss-associated S1PR2 variants.
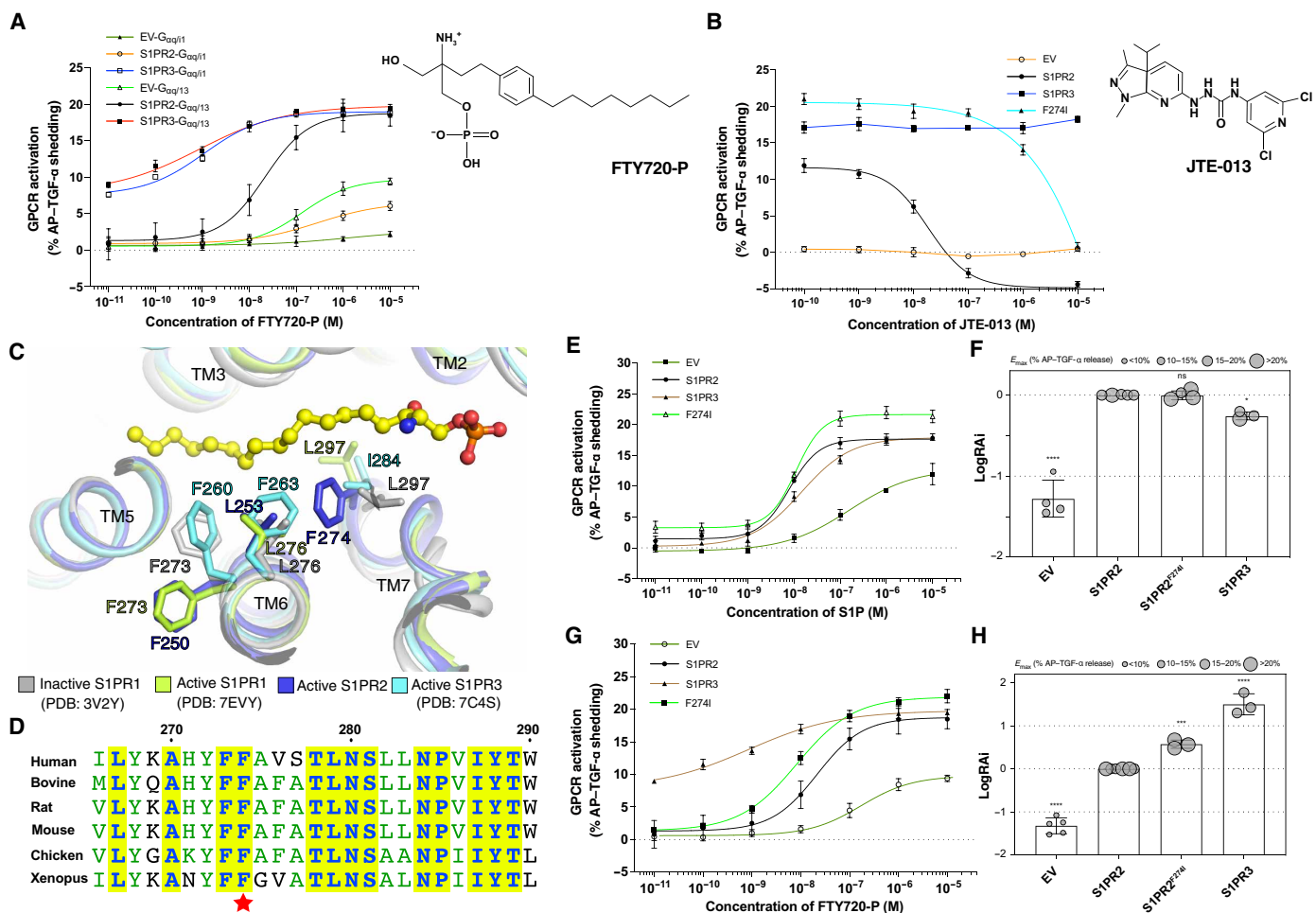
Fig. 5. FTY720-P triggers G$_{13}$ activation via S1PR2. (**A**) Dose-response curves of S1PR2 and S1PR3 for the TGFα shedding assay using FTY720-P. The chemical structure of FTY720-P is shown. Data are means ± SD (*n* = 3). The membrane expression of S1PRs is shown in figs. S4A and S6C. EV, empty vector. (**B**) JTE-013 reduces the FTY720-P–induced activation of S1PR2 but not S1PR3. The chemical structure of JTE-013 is shown. Data are means ± SD (*n* = 3). (**C**) Structural comparisons among S1PRs imply the unique roles of residue F274 of S1PR2. The residues are shown in sticks. (**D**) The sequence alignment of S1PR2-TM7 from different species. The conserved residues are highlighted. The residue F274 is indicated by a star. (**E** and **G**) Mutagenesis analysis of S1PR2^{F274I} for S1P (E) and FTY720-P (G). The representative dose-response curves from same-day experiment are shown. Data are means ± SD (*n* = 3). (**F** and **H**) RAi of each varient for S1P (F) and FTY720-P (H). Each LogRAi plot denotes a single measurement from a dose-response experiment. Data are means ± SD (*n* = 3 to 5 independent experiments). *$P < 0.05$, ***$P < 0.001$, and ****$P < 0.0001$; mutant versus wild-type values according to one-way ANOVA with Dunnett's multiple comparison test.

The therapeutic agent FTY720 has been used to treat auto-immune disease in more than 300,000 people (*10*). Low activity of the drug on S1PR2 is thought to be crucial in avoiding unwanted effects on the immune, vascular, and auditory systems. At the recommended daily dose for treatment of multiple sclerosis of 0.5 mg, the steady-state blood FTY720-P concentration is estimated to reach ~1 ng/ml (~2.6 nM) (*61*). The drug target, S1PR1, is functionally antagonized by low-nanomolar concentrations of FTY720-P (*44*), while 100- to 1000-fold greater amounts are needed to have strong functional effects on S1PR2 [this study and (*48*)]. Thus, at the approved dosing, the drug is unlikely to interfere with S1PR2 function. In rodent studies, however, it is common to use a dose of 1 mg/kg. A linear extrapolation from 0.5-mg daily dosing in a 70-kg human would suggest that an FTY720-P concentration of 360 nM may be reached in rodents treated with FTY720 (1 mg/kg) daily. The possible influence of FY720-P agonism of S1PR2 needs to be considered

when interpreting in vivo effects of FTY720 treatment of rodents in this dose range. The suggestion in early studies that FTY720-P does not engage S1PR2 may have been a consequence of the low signal-to-noise ratio in binding assays, making it challenging to detect weak interactions. By revealing conserved features of the S1PR2 binding pocket that interfere with FTY720-P signaling, this work enables improved structure-guided drug design efforts for next-generation S1PR1 targeting therapeutics. S1PR2 signaling via G$_{α12/13}$ and Rho in endothelial cells reduces junctional integrity and promotes vascular permeability (*16*). In models of multiple sclerosis, acute lung injury, and endotoxemia, S1PR2 signaling contributes to endothelial leakiness and disease (*16, 62–64*). In myeloid cells, S1PR2 activation suppresses macrophage migration and promotes their retention in pathological lesions (*65, 66*). In toxin-induced liver and lung damage, S1PR2 signaling impedes tissue regeneration and increases fibrosis (*67, 68*). Development of new classes of S1PR2 antagonists as potential
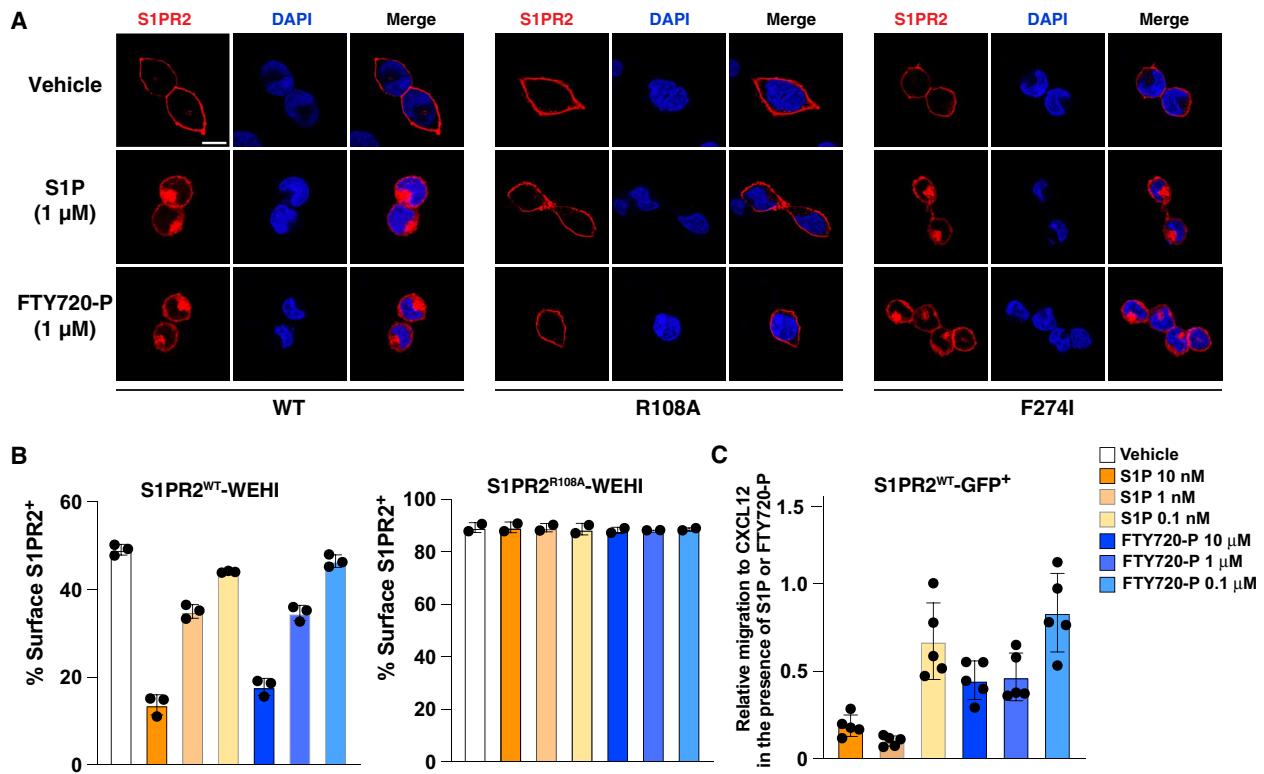
Fig. 6. The S1PR2 internalization assays. (**A**) The immunofluorescence staining of HEK293 cells that express S1PR2 or its variants after vehicle or 1 μM ligand treatment. Scale bar, 10 μm. DAPI, 4′,6-diamidino-2-phenylindole. (**B**) Internalization of S1PR2^{WT} or S1PR2^{R108A} in WEHI-231 cells in response to the indicated amounts of S1P or FTY720-P treatment. Graphs show percent cells with detectable S1PR2 surface staining determined using flow cytometry. (**C**) Cell migration inhibition assay with S1PR2^{WT} WEHI-231 cells in response to S1P or FTY720-P at the indicated concentrations. Data are means ± SD (pooled from three independent experiments).

therapeutics to treat these conditions will be aided by this S1PR2-G$_{\alpha 13}$ structure.

MATERIALS AND METHODS
Protein expression, purification, and assembly of hS1PR2-G$_{13}$-scFv16 complex

The full-length cDNA of wild-type human S1PR2 (UniProt: O95136) was cloned into pEG-BacMam vector with a C-terminal FLAG tag. The protein was expressed using baculovirus-mediated transduction of mammalian HEK293S GnTI$^-$ cells [American Type Culture Collection (ATCC)]. Baculovirus was generated in Sf9 cells (ATCC), and P2 virus was used to infect HEK293S GnTI$^-$ cells at 37°C. At 8 hours after infection, sodium butyrate at a final concentration of 10 mM was added to the culture. After further incubation for 60 hours at 30°C, cells were harvested and resuspended in buffer A [20 mM Hepes (pH 7.5) and 150 mM NaCl] supplemented with 1 mM phenylmethylsulfonyl fluoride, leupeptin (10 μg/ml), and 5 μM S1P and then homogenized by sonication. The lysate was cleared by centrifugation at 3000g for 5 min at 4°C. The resulting supernatant was supplemented with 1% L-MNG (lauryl maltose neopentyl glycol) /0.1% CHS (cholesteryl hemisuccinate) and incubated for 1 hour at 4°C. Insoluble components were removed by centrifugation at 40,000g, 4°C for 30 min, and the clarified lysate was then loaded onto a disposable gravity column (Bio-Rad) containing anti-FLAG M2 affinity agarose resin (Sigma-Aldrich). After washing two times with 10 column volumes (CVs) of buffer B [20 mM Hepes (pH 7.5), 150 mM NaCl, 0.01%

L-MNG/0.001% CHS, and 5 μM S1P], the protein was eluted with 4 CVs of buffer B supplemented with 3× FLAG peptide (0.1 mg/ml; ApexBio). The eluted protein was further purified by size exclusion chromatography using a Superose 6 Increase 10/300 GL column (Cytiva) preequilibrated with buffer C [20 mM Hepes (pH 7.5), 150 mM NaCl, 0.001% L-MNG/0.0001% CHS, and 0.0025% GDN (glyco-diosgenin)] with 5 μM S1P. The peak fractions were collected for complex assembly.

For expression of chimeric G$_{13iN}$, a DNA fragment encoding amino acid residues 1 to 31 of human Gα$_{i1}$ was fused to the N terminus of human Gα$_{13}$ (residues 47 to 377) and cloned into the expression vector pFastBac1 without any tag. The cDNAs of wild-type human β1γ2 subunits were cloned into pFastBac Dual vector with a 6×His tag inserted at the N terminus of the β1 subunit. The expression and purification of heterotrimeric G$_{13iN}$ protein were performed on the basis of a published method that was used for purifying heterotrimeric G$_i$ (69). scFv16 was expressed and purified as previously described (31).

To assemble the S1PR2-G$_{13}$-scFv16 complex, purified S1PR2 was mixed with the G$_{13}$ heterotrimer at a 1:1.2 molar ratio. This mixture was incubated on ice for 1 hour, followed by the addition of apyrase to catalyze the hydrolysis of unbound GDP on ice for 1 hour. Then, scFv16 was added at a 1.5:1 molar ratio (scFv16: S1PR2) followed by 30-min incubation on ice. The mixture was diluted 10-fold by buffer C containing 5 μM S1P. To remove excess G$_{13}$ and scFv16 proteins, the mixture was purified by anti-FLAG M2 antibody affinity chromatography in the presence of 5 μM S1P. The complex was eluted in buffer C supplemented with 5 μM S1P and 3×FLAG peptide

(0.1 mg/ml). After concentration, the complex was further purified by size exclusion chromatography (Superose 6 Increase 10/300 GL) in buffer C with 5 μM S1P. Peak fractions were concentrated to ~10 to 12 mg/ml for cryo-EM studies.

Cryo-EM sample preparation and data acquisition

The freshly purified hS1PR2-G$_{13}$-scFv16 complex was added to Quantifoil R1.2/1.3 400-mesh Au holey carbon grids (Quantifoil), blotted using a Vitrobot Mark IV (FEI), and frozen in liquid ethane. The grids were imaged in a 300-keV Titan Krios (FEI) with a Gatan K3 Summit direct electron detector. Data were collected in super-resolution mode at a pixel size of 0.421 Å with a dose rate of 23 electrons per physical pixel per second. Images were recorded for 1.8-s exposures in 60 subframes to give a total dose of 60 electrons/Å^2.

Imaging processing and 3D reconstruction

A total of four datasets with 6696, 9876, 11,259, and 5349 micrographs, respectively, were collected. For each dataset, dark subtracted images were normalized by gain reference and binned twofold that resulted in the original pixel size of 0.842 Å. Drift correction was performed using the program MotionCor2 (70). The contrast transfer function (CTF) was estimated using CTFFIND4 (71). For the first dataset, about 2000 particles were manually picked and classified by 2D classification in RELION-3. The 2D class averages were used as the templates for autopicking in RELION-3 (72). After autopicking in RELION, the particles were extracted with a pixel size of 2.526 Å. The extracted particles were imported into cryoSPARC (73) for 2D classification followed by ab initio reconstruction with a class number of 5. The resulting ab initio maps and the cryo-EM map of SMO-Gi complex (EMD-22120) (37) were used as models in the following parallel heterogeneous refinements. The particles from heterogeneous refinements were combined, and duplicated particles were removed. Then, the resulting particles were transformed into RELION format, and one round of 3D classification was performed. The particles from the best class were recentered and reextracted with a pixel size of 0.842 Å and imported into cryoSPARC for further parallel heterogeneous refinements with various class number ($K = 3, 4, 5,$ and 6). The resulting particles were combined, deduplicated, transformed into RELION format, and subjected to another round of 3D classification followed by 3D refinement and Bayesian polishing, which gave rise to a reconstruction at the resolution of 4.41 Å. For the other three datasets, a similar procedure was applied with the exception that 2D references were made by projection of 3D map generated from the first dataset. The resulting 123,752, 242,485, 335,498, and 150,558 particles from all four datasets were then combined and imported into cryoSPARC for further 2D classification and heterogeneous refinement with a class number of 2. A final number of 640,483 particles were selected from the better class and subjected to nonuniform refinement and local CTF refinement, which gave rise to a final reconstruction at the resolution of 3.19 Å using the 0.143 cutoff criteria. Local resolutions were estimated using cryoSPARC.

Model construction and refinement

The cryo-EM structure of the CB1-G$_i$ [Protein Data Bank (PDB): 6N4B] (74) and the crystal structure of chimeric Gα$_{i/13}$ (PDB: 1ZCB) (28) together with a homology model of S1PR2 were used as initial models and manually docked into cryo-EM density map with Chimera (75). The resulting model was subjected to iterative rounds of manual adjustment and rebuilding in Coot (76) and refinement using Phenix

real-space refine (77). The model of the ligand S1P was manually built in Coot. MolProbity (78) was used to validate the geometries of the model. Structural figures were generated using PyMOL (www.pymol.org) and Chimera.

TGF-α shedding assay

The cDNAs encoding human S1PR2 and S1PR3 were cloned into the pCAGGS expression vector followed by a FLAG epitope tag at their C terminus. Point mutations of S1PR2 were introduced by two-step overlapping polymerase chain reaction. HEK293 ΔG$_{q/11/12/13}$ cell line (79) was a gift from A. Inoue at the Tohoku University, Japan. The cells were maintained in Dulbecco's modified Eagle's medium–low glucose (DMEM-LG; Sigma-Aldrich) supplemented with heat-inactivated fetal calf serum and penicillin-streptomycin (100 U/ml and 100 μg/ml, Corning) at 37°C in a 5% CO$_2$ incubator.

The TGF-α shedding assay was performed as described previously (11, 23). HEK293 ΔG$_{q/11/12/13}$ cells were seeded in a 12-well plate at a density of 1×10^5 cells per well in 1 ml of DMEM-LG supplemented with 10% charcoal-stripped fetal bovine serum (Gibco) and penicillin-streptomycin and cultured at 37°C with 5% CO$_2$ for 24 hours. Transient transfection was performed with a mixture of AP–TGF-α–encoding plasmid (250 ng per well, hereafter), S1PR2- or S1PR3-encoding plasmid (100 ng), and Gα-encoding plasmid using 1.2 μl of FuGene 6 transfection reagent (Promega). After 24 hours, the transfected cells were detached with 0.05% Trypsin-EDTA solution (Gibco) followed by adding complete DMEM to inactivate trypsin. The cells were palleted by centrifugation at 200g for 5 min and resuspended in 4 ml of Hanks' balanced salt solution (HBSS) with calcium and magnesium (Gibco) containing 5 mM Hepes (pH 7.4). After incubation at room temperature for 10 min, cells were palleted by centrifugation and resuspended in 2.5 ml of Hepes-containing HBSS. The cell suspension was seeded into a 96-well culture plate with lid at a volume of 90 μl per well and incubated at 37°C in a 5% CO$_2$ incubator for 30 min. The ligand S1P (Tocris) or FTY720 (S)-phosphate (FTY720-P, Echelon) was serially diluted in HBSS supplemented with 5 mM Hepes (pH 7.4) and 0.01% fatty acid–free bovine serum albumin (BSA; GoldBio) to prepare 10× stock solutions. The cells of each well were treated with 10 μl of ligand stock solution, where each concentration was tested in triplicate, and further incubated for 1 hour. Then, the plates were centrifuged at 400g for 5 min, and 80 μl of conditioned medium (CM) was transferred to a new 96-well culture plate. For each well of both cell plate and CM plate, 80 μl of AP reaction solution [120 mM tris-HCl (pH 9.5), 40 mM NaCl, 10 mM MgCl$_2$, and 10 mM p-nitrophenyl phosphate (Thermo Fisher Scientific)] was added, and the absorbance at 405 nm (A) was measured using a microplate reader (Synergy Neo2, BioTek). After incubation at room temperature for 2 hours, the absorbance at 405 nm (A') was measured again to get the AP activity ($\Delta A = A' - A$). S1P- or FTY720-P–induced AP–TGF-α release was calculated as described previously (30). AP–TGF-α release signal over ligand concentration was fitted to a four-parameter logistic sigmoidal curve using Prism 9 software (GraphPad), from which EC$_{50}$ and E_{max} values were obtained. For JTE-013 inhibition experiment, JTE-013 was serially diluted in HBSS with 5 mM Hepes (pH 7.4) and 0.01% fatty acid–free BSA in the presence or absence of 1 μM FTY720-P.

Migration inhibition transwell bioassays

S1PR2 and GNA13 wild-type and point mutant retroviral constructs were made by inserting the human open reading frame into the

MSCV2.2 retroviral vector followed by an internal ribosome entry site and Thy1.1 or green fluorescent protein (GFP) as an expression marker. For S1PR2 constructs, an OX56 (rat CD43-derived) epitope was included at the N terminus to track surface expression levels of each receptor using the OX56 antibody (80). The retrovirus-encoding S1PR2 or GNA13 wild-type or point mutants were produced using the Platinum-E packaging cell line. Approximately 1×10^6 WEHI-231 or M12 cells were placed in a six-well plate along with the retroviral supernatant, and the cells were centrifuged at 1340g (2400 rpm) for 2 hours at room temperature. The viral supernatant was aspirated, and the cells were resuspended in growth medium and returned to culture. This spinfection was repeated with fresh retrovirus for a second time 24 hours later. Forty-eight hours after the second spinfection, the cells were analyzed on flow cytometry for the percentage of GFP- or Thy1.1-expressing cells. Cells were cultured to confluency in T75 flasks before use in transwell bioassays.

For transwell bioassays, transduced WEHI-231 or M12 cells were washed twice in prewarmed migration medium (RPMI 1640 containing 0.5% fatty acid–free BSA, 10 mM Hepes, and 50 IU of penicillin/streptomycin). The cells were resuspended in migration medium at 2.5×10^6 cells/ml and incubated for 20 min in a 37°C water bath. Recombinant human CXCL12 (PeproTech) was diluted to 100 ng/ml in migration medium. S1P (d18:1) (Avanti Polar Lipids) was diluted to 1 nM in CXCL12-containing migration medium. Alternatively, FTY720-P was diluted to 0.1 µM in an equivalent way. Six hundred microliters of each of these mixtures was added to a 24-well tissue culture plate. Transwell filters (6-mm insert, 5-µm pore size; Corning) were placed on top of each well, and 100 µl of transduced WEHI-231 or M12 cells (2.5×10^5 cells) was added to the transwell insert. The cells were allowed to migrate for 3 hours, after which the cells in the bottom well were counted by flow cytometry. To assess migration inhibition, the proportion of S1PR2-GFP$^+$ or G$_{13}$-Thy1.1$^+$ cells that migrated to CXCL12 with S1P was divided by the proportion of S1PR2-GFP$^+$ or G$_{13}$-Thy1.1$^+$ cells that migrated to CXCL12 alone.

Internalization assay in WEHI-231 cells
WEHI-231 cells expressing OX56-S1PR2-GFP were prepared as for the cell migration assays, and then, 40 µl of medium containing 2×10^5 cells was placed in each well of a round bottom 96-well plate. Appropriately diluted S1P or FTY720-P (160 µl) prepared in migration medium was added, and the plate was incubated at 37°C for 60 min. The fraction of GFP$^+$ cells that were stained for OX56 was then determined by flow cytometry. Gates used for OX56 staining were set on the basis of GFP$^-$ cells.

Antibodies used for analyzing G$\alpha_{q/13}$ expression level
Anti-Gαq mouse monoclonal antibody (Santa Cruz Biotechnology, catalog no. sc-136181) was used for detecting the expression level of G$_{\alpha q/13}$ protein and its mutants. Anti–β-tubulin mouse monoclonal antibody (Cell Signaling Technology, catalog no. 86298S) was used for normalizing the amount of loaded sample. Anti-mouse immunoglobulin G (IgG) secondary antibody conjugated with horseradish peroxidase was from Cell Signaling Technology (catalog no. 7076S). Similar results were obtained in three biologically independent experiments.

Immunofluorescence staining
HEK293 ΔG$_{q/11/12/13}$ cells were seeded on poly-D-lysine–coated coverslips in 24-well plates and transfected with plasmids of wild-type or mutant

S1PR2 (or S1PR3) as used in the above TGF-α shedding assay. At 24 hours after transfection, the cells were fixed with 4% paraformaldehyde in phosphate-buffered saline (PBS) for 15 min, permeabilized with 100% methanol (prechilled at −20°C) for 5 min, blocked with 2% BSA in PBS for 1 hour, and labeled with anti-FLAG mouse antibody (2 µg/ml; Sigma-Aldrich, catalog no. F1804-50UG) for 3 hours at room temperature. Donkey anti-mouse IgG secondary antibody conjugated with Alexa Fluor 568 (Thermo Fisher Scientific, catalog no. A10037) was used at a concentration of 2 µg/ml in blocking buffer for 1 hour at room temperature for detection of FLAG-tagged S1PR2 or S1PR3. The coverslips were mounted onto glass slides with antifade reagent with 4′,6-diamidino-2-phenylindole (Thermo Fisher Scientific, catalog no. P36931). Fluorescence images were acquired using a Zeiss LSM 800 microscope system with ZEN imaging software (Zeiss). For internalization analysis, transfected HEK293 cells were serum-starved for 1 hour before S1P or FTY720-P treatment. After treatment for 1 hour, the cells were subjected to fixation, immunostaining, and imaging as described above. Similar results were obtained in three biologically independent experiments.

REFERENCES AND NOTES
1. E. Lu, J. G. Cyster, G-protein coupled receptors and ligands that organize humoral immune responses. *Immunol. Rev.* **289**, 158–172 (2019).
2. H. Mizuno, Y. Kihara, Druggable lipid GPCRs: Past, present, and prospects. *Adv. Exp. Med. Biol.* **1274**, 223–258 (2020).
3. X. Qi, X. Li, Mechanistic insights into the generation and transduction of hedgehog signaling. *Trends Biochem. Sci.* **45**, 397–410 (2020).
4. S. Spiegel, S. Milstien, Sphingosine-1-phosphate: An enigmatic signalling lipid. *Nat. Rev. Mol. Cell Biol.* **4**, 397–407 (2003).
5. A. Cartier, T. Hla, Sphingosine 1-phosphate: Lipid signaling in pathology and therapy. *Science* **366**, (2019).
6. H. Rosen, R. C. Stevens, E. Hanson, E. Roberts, M. B. A. Oldstone, Sphingosine-1-phosphate and its receptors: Structure, signaling, and influence. *Annu. Rev. Biochem.* **82**, 637–662 (2013).
7. R. L. Proia, T. Hla, Emerging biology of sphingosine-1-phosphate: Its role in pathogenesis and therapy. *J. Clin. Invest.* **125**, 1379–1387 (2015).
8. L. Kappos, E. W. Radue, P. O'Connor, C. Polman, R. Hohlfeld, P. Calabresi, K. Selmaj, C. Agoropoulou, M. Leyk, L. Zhang-Auberson, P. Burtin; FREEDOMS Study Group, A placebo-controlled trial of oral fingolimod in relapsing multiple sclerosis. *N. Engl. J. Med.* **362**, 387–401 (2010).
9. V. Brinkmann, A. Billich, T. Baumruker, P. Heining, R. Schmouder, G. Francis, S. Aradhye, P. Burtin, Fingolimod (FTY720): Discovery and development of an oral drug to treat multiple sclerosis. *Nat. Rev. Drug Discov.* **9**, 883–897 (2010).
10. J. Chun, G. Giovannoni, S. F. Hunter, Sphingosine 1-phosphate receptor modulator therapy for multiple sclerosis: Differential downstream receptor signalling and clinical profile effects. *Drugs* **81**, 207–231 (2021).
11. A. Inoue, F. Raimondi, F. M. N. Kadji, G. Singh, T. Kishi, A. Uwamizu, Y. Ono, Y. Shinjo, S. Ishida, N. Arang, K. Kawakami, J. S. Gutkind, J. Aoki, R. B. Russell, Illuminating G-protein-coupling selectivity of GPCRs. *Cell* **177**, 1933–1947.e25 (2019).
12. N. Sugimoto, N. Takuwa, H. Okamoto, S. Sakurada, Y. Takuwa, Inhibitory and stimulatory regulation of Rac and cell motility by the G12/13-Rho and Gi pathways integrated downstream of a single G protein-coupled sphingosine-1-phosphate receptor isoform. *Mol. Cell. Biol.* **23**, 1534–1545 (2003).
13. R. T. Windh, M.-J. Lee, T. Hla, S. An, A. J. Barr, D. R. Manning, Differential coupling of the sphingosine 1-phosphate receptors Edg-1, Edg-3, and H218/Edg-5 to the G$_i$, G$_q$, and G$_{12}$ families of heterotrimeric G proteins. *J. Biol. Chem.* **274**, 27351–27358 (1999).
14. J. A. Green, K. Suzuki, B. Cho, L. D. Willison, D. Palmer, C. D. C. Allen, T. H. Schmidt, Y. Xu, R. L. Proia, S. R. Coughlin, J. G. Cyster, The sphingosine 1-phosphate receptor S1P$_2$ maintains the homeostasis of germinal center B cells and promotes niche confinement. *Nat. Immunol.* **12**, 672–680 (2011).

15. J. R. Muppidi, R. Schmitz, J. A. Green, W. Xiao, A. B. Larsen, S. E. Braun, J. An, Y. Xu, A. Rosenwald, G. Ott, R. D. Gascoyne, L. M. Rimsza, E. Campo, E. S. Jaffe, J. Delabie, E. B. Smeland, R. M. Braziel, R. R. Tubbs, J. R. Cook, D. D. Weisenburger, W. C. Chan, N. Vaidehi, L. M. Staudt, J. G. Cyster, Loss of signalling via Gα13 in germinal centre B-cell-derived lymphoma. *Nature* **516**, 254–258 (2014).

16. Y. Takuwa, Y. Okamoto, K. Yoshioka, N. Takuwa, Sphingosine-1-phosphate signaling in physiology and diseases. *Biofactors* **38**, 329–337 (2012).

17. R. L. Santos-Cortez, R. Faridi, A. U. Rehman, K. Lee, M. Ansar, X. Wang, R. J. Morell, R. Isaacson, I. A. Belyantseva, H. Dai, A. Acharya, T. A. Qaiser, D. Muhammad, R. A. Ali, S. Shams, M. J. Hassan, S. Shahzad, S. I. Raza, Z. E. Bashir, J. D. Smith, D. A. Nickerson, M. J. Bamshad; University of Washington Center for Mendelian Genomics, S. Riazuddin, W. Ahmad, T. B. Friedman, S. M. Leal, Autosomal-recessive hearing impairment due to rare missense variants within S1PR2. *Am. J. Hum. Genet.* **98**, 331–338 (2016).

18. M. A. H. Hofrichter, M. Mojarad, J. Doll, C. Grimm, A. Eslahi, N. S. Hosseini, M. Rajati, T. Müller, M. Dittrich, R. Maroofian, T. Haaf, B. Vona, The conserved p.Arg108 residue in S1PR2 (DFNB68) is fundamental for proper hearing: Evidence from a consanguineous Iranian family. *BMC Med. Genet.* **19**, 81 (2018).

19. R. D. Morin, M. Mendez-Lago, A. J. Mungall, R. Goya, K. L. Mungall, R. D. Corbett, N. A. Johnson, T. M. Severson, R. Chiu, M. Field, S. Jackman, M. Krzywinski, D. W. Scott, D. L. Trinh, J. Tamura-Wells, S. Li, M. R. Firme, S. Rogic, M. Griffith, S. Chan, O. Yakovenko, I. M. Meyer, E. Y. Zhao, D. Smailus, M. Moksa, S. Chittaranjan, L. Rimsza, A. Brooks-Wilson, J. J. Spinelli, S. Ben-Neriah, B. Meissner, B. Woolcock, M. Boyle, H. McDonald, A. Tam, Y. Zhao, A. Delaney, T. Zeng, K. Tse, Y. Butterfield, I. Birol, R. Holt, J. Schein, D. E. Horsman, R. Moore, S. J. M. Jones, J. M. Connors, M. Hirst, R. D. Gascoyne, M. A. Marra, Frequent mutation of histone-modifying genes in non-Hodgkin lymphoma. *Nature* **476**, 298–303 (2011).

20. J. G. Lohr, P. Stojanov, M. S. Lawrence, D. Auclair, B. Chapuy, C. Sougnez, P. Cruz-Gordillo, B. Knoechel, Y. W. Asmann, S. L. Slager, A. J. Novak, A. Dogan, S. M. Ansell, B. K. Link, L. Zou, J. Gould, G. Saksena, N. Stransky, C. Rangel-Escareno, J. C. Fernandez-Lopez, A. Hidalgo-Miranda, J. Melendez-Zajgla, E. Hernandez-Lemus, A. Schwarz-Cruz y Celis, I. Imaz-Rosshandler, A. I. Ojesina, J. Jung, C. S. Pedamallu, E. S. Lander, T. M. Habermann, J. R. Cerhan, M. A. Shipp, G. Getz, T. R. Golub, Discovery and prioritization of somatic mutations in diffuse large B-cell lymphoma (DLBCL) by whole-exome sequencing. *Proc. Natl. Acad. Sci. U.S.A.* **109**, 3879–3884 (2012).

21. R. D. Morin, K. Mungall, E. Pleasance, A. J. Mungall, R. Goya, R. D. Huff, D. W. Scott, J. Ding, A. Roth, R. Chiu, R. D. Corbett, F. C. Chan, M. Mendez-Lago, D. L. Trinh, M. Bolger-Munro, G. Taylor, A. Hadj Khodabakhshi, S. Ben-Neriah, J. Pon, B. Meissner, B. Woolcock, N. Farnoud, S. Rogic, E. L. Lim, N. A. Johnson, S. Shah, S. Jones, C. Steidl, R. Holt, I. Birol, R. Moore, J. M. Connors, R. D. Gascoyne, M. A. Marra, Mutational and structural analysis of diffuse large B-cell lymphoma using whole-genome sequencing. *Blood* **122**, 1256–1265 (2013).

22. M. A. Hanson, C. B. Roth, E. Jo, M. T. Griffith, F. L. Scott, G. Reinhart, H. Desale, B. Clemons, S. M. Cahalan, C. Schuerer, M. G. Sanna, G. W. Han, P. Kuhn, H. Rosen, R. C. Stevens, Crystal structure of a lipid G protein-coupled receptor. *Science* **335**, 851–855 (2012).

23. S. Maeda, Y. Shiimura, H. Asada, K. Hirata, F. Luo, E. Nango, N. Tanaka, M. Toyomoto, A. Inoue, J. Aoki, S. Iwata, M. Hagiwara, Endogenous agonist–bound S1PR3 structure reveals determinants of G protein–subtype bias. *Sci. Adv.* **7**, eabf5325 (2021).

24. Y. Yuan, G. Jia, C. Wu, W. Wang, L. Cheng, Q. Li, Z. Li, K. Luo, S. Yang, W. Yan, Z. Su, Z. Shao, Structures of signaling complexes of lipid receptors S1PR1 and S1PR5 reveal mechanisms of activation and drug recognition. *Cell Res.* **31**, 1263–1274 (2021).

25. C. Zhao, L. Cheng, W. Wang, H. Wang, Y. Luo, Y. Feng, X. Wang, H. Fu, Y. Cai, S. Yang, P. Fu, W. Yan, Z. Shao, Structural insights into sphingosine-1-phosphate recognition and ligand selectivity of S1PR3–Gi signaling complexes. *Cell Res.* **32**, 218–221 (2022).

26. T. Worzfeld, N. Wettschureck, S. Offermanns, G$_{12}$/G$_{13}$-mediated signalling in mammalian physiology and disease. *Trends Pharmacol. Sci.* **29**, 582–589 (2008).

27. S. Maeda, Q. Qu, M. J. Robertson, G. Skiniotis, B. K. Kobilka, Structures of the M1 and M2 muscarinic acetylcholine receptor/G-protein complexes. *Science* **364**, 552–557 (2019).

28. B. Kreutz, D. M. Yau, M. R. Nance, S. Tanabe, J. J. G. Tesmer, T. Kozasa, A new approach to producing functional Gα subunits yields the activated and deactivated structures of Gα$_{12/13}$ proteins. *Biochemistry* **45**, 167–174 (2006).

29. S. Maeda, A. Koehl, H. Matile, H. Hu, D. Hilger, F. X. Schertler, A. Manglik, G. Skiniotis, R. J. P. Dawson, B. K. Kobilka, Development of an antibody fragment that stabilizes GPCR/G-protein complexes. *Nat. Commun.* **9**, 3712 (2018).

30. A. Inoue, J. Ishiguro, H. Kitamura, N. Arima, M. Okutani, A. Shuto, S. Higashiyama, T. Ohwada, H. Arai, K. Makide, J. Aoki, TGFα shedding assay: An accurate and versatile method for detecting GPCR activation. *Nat. Methods* **9**, 1021–1029 (2012).

31. A. Koehl, H. Hu, S. Maeda, Y. Zhang, Q. Qu, J. M. Paggi, N. R. Latorraca, D. Hilger, R. Dawson, H. Matile, G. F. X. Schertler, S. Granier, W. I. Weis, R. O. Dror, A. Manglik, G. Skiniotis, B. K. Kobilka, Structure of the μ-opioid receptor-Gi protein complex. *Nature* **558**, 547–552 (2018).

32. S. G. Rasmussen, B. T. De Vree, Y. Zou, A. C. Kruse, K. Y. Chung, T. S. Kobilka, F. S. Thian, P. S. Chae, E. Pardon, D. Calinski, J. M. Mathiesen, S. T. A. Shah, J. A. Lyons, M. Caffrey, S. H. Gellman, J. Steyaert, G. Skiniotis, W. I. Weis, R. K. Sunahara, B. K. Kobilka, Crystal structure of the β$_2$ adrenergic receptor-Gs protein complex. *Nature* **477**, 549–555 (2011).

33. B. T. DeVree, J. P. Mahoney, G. A. Vélez-Ruiz, S. G. F. Rasmussen, A. J. Kuszak, E. Edward, J. J. Fung, A. Manglik, M. Masureel, Y. du, R. A. Matt, E. Pardon, J. Steyaert, B. K. Kobilka, R. K. Sunahara, Allosteric coupling from G protein to the agonist-binding pocket in GPCRs. *Nature* **535**, 182–186 (2016).

34. W. I. Weis, B. K. Kobilka, The molecular basis of G protein-coupled receptor activation. *Annu. Rev. Biochem.* **87**, 897–919 (2018).

35. Q. Zhou, D. Yang, M. Wu, Y. Guo, W. Guo, L. Zhong, X. Cai, A. Dai, W. Jang, E. I. Shakhnovich, Z.-J. Liu, R. C. Stevens, N. A. Lambert, M. M. Babu, M.-W. Wang, S. Zhao, Common activation mechanism of class A GPCRs. *eLife* **8**, e50279 (2019).

36. I. Deshpande, J. Liang, D. Hedeen, K. J. Roberts, Y. Zhang, B. Ha, N. R. Latorraca, B. Faust, R. O. Dror, P. A. Beachy, B. R. Myers, A. Manglik, Smoothened stimulation by membrane sterols drives Hedgehog pathway activity. *Nature* **571**, 284–288 (2019).

37. X. Qi, L. Friedberg, R. De Bose-Boyd, T. Long, X. Li, Sterols in an intramolecular channel of Smoothened mediate Hedgehog signaling. *Nat. Chem. Biol.* **16**, 1368–1375 (2020).

38. V. Katritch, V. Cherezov, R. C. Stevens, Structure-function of the G protein-coupled receptor superfamily. *Annu. Rev. Pharmacol. Toxicol.* **53**, 531–556 (2013).

39. H. Obinata, T. Hla, Sphingosine 1-phosphate and inflammation. *Int. Immunol.* **31**, 617–625 (2019).

40. T. Flock, A. S. Hauser, N. Lund, D. E. Gloriam, S. Balaji, M. M. Babu, Selectivity determinants of GPCR-G-protein binding. *Nature* **545**, 317–322 (2017).

41. M. Su, L. Zhu, Y. Zhang, N. Paknejad, R. Dey, J. Huang, M.-Y. Lee, D. Williams, K. D. Jordan, E. T. Eng, O. P. Ernst, J. R. Meyerson, R. K. Hite, T. Walz, W. Liu, X.-Y. Huang, Structural basis of the activation of heterotrimeric Gs-protein by isoproterenol-bound β$_1$-adrenergic receptor. *Mol. Cell* **80**, 59–71.e4 (2020).

42. S. W. Paugh, S. G. Payne, S. E. Barbour, S. Milstien, S. Spiegel, The immunosuppressant FTY720 is phosphorylated by sphingosine kinase type 2. *FEBS Lett.* **554**, 189–193 (2003).

43. K. Chiba, FTY720, a new class of immunomodulator, inhibits lymphocyte egress from secondary lymphoid tissues and thymus by agonistic activity at sphingosine 1-phosphate receptors. *Pharmacol. Ther.* **108**, 308–319 (2005).

44. S. Mandala, R. Hajdu, J. Bergstrom, E. Quackenbush, J. Xie, J. Milligan, R. Thornton, G.-J. Shei, D. Card, C.-A. Keohane, M. Rosenbach, J. Hale, C. L. Lynch, K. Rupprecht, W. Parsons, H. Rosen, Alteration of lymphocyte trafficking by sphingosine-1-phosphate receptor agonists. *Science* **296**, 346–349 (2002).

45. V. Brinkmann, M. D. Davis, C. E. Heise, R. Albert, S. Cottens, R. Hof, C. Bruns, E. Prieschl, T. Baumruker, P. Hiestand, C. A. Foster, M. Zollinger, K. R. Lynch, The immune modulator FTY720 targets sphingosine 1-phosphate receptors. *J. Biol. Chem.* **277**, 21453–21457 (2002).

46. S. C. Sensken, C. Stäubert, P. Keul, B. Levkau, T. Schöneberg, M. H. Gräler, Selective activation of G alpha i mediated signalling of S1P3 by FTY720-phosphate. *Cell. Signal.* **20**, 1125–1133 (2008).

47. K. Sobel, L. Monnier, K. Menyhart, M. Bolinger, R. Studer, O. Nayler, J. Gatfield, FTY720 Phosphate activates sphingosine-1-phosphate receptor 2 and selectively couples to Gα12/13/Rho/ROCK to induce myofibroblast contraction. *Mol. Pharmacol.* **87**, 916–927 (2015).

48. J. A. Wetter, C. Revankar, B. J. Hanson, Utilization of the Tango™ β-Arrestin recruitment technology for cell-based EDG receptor assay development and interrogation. *J. Biomol. Screen.* **14**, 1134–1141 (2009).

49. M. Osada, Y. Yatomi, T. Ohmori, H. Ikeda, Y. Ozaki, Enhancement of sphingosine 1-phosphate-induced migration of vascular endothelial cells and smooth muscle cells by an EDG-5 antagonist. *Biochem. Biophys. Res. Commun.* **299**, 483–487 (2002).

50. J. Xu, F. Wang, A. van Keymeulen, P. Herzmark, A. Straight, K. Kelly, Y. Takuwa, N. Sugimoto, T. Mitchison, H. R. Bourne, Divergent signals and cytoskeletal assemblies regulate self-organizing polarity in neutrophils. *Cell* **114**, 201–214 (2003).

51. G. Cinamon, M. Matloubian, M. J. Lesneski, Y. Xu, C. Low, T. Lu, R. L. Proia, J. G. Cyster, Sphingosine 1-phosphate receptor 1 promotes B cell localization in the splenic marginal zone. *Nat. Immunol.* **5**, 713–720 (2004).

52. P. Keul, S. Lucke, K. von Wnuck Lipinski, C. Bode, M. Gräler, G. Heusch, B. Levkau, Sphingosine-1-phosphate receptor 3 promotes recruitment of monocyte/macrophages in inflammation and atherosclerosis. *Circ. Res.* **108**, 314–323 (2011).

53. B. J. Laidlaw, E. E. Gray, Y. Zhang, F. Ramirez-Valle, J. G. Cyster, Sphingosine-1-phosphate receptor 2 restrains egress of γδ T cells from the skin. *J. Exp. Med.* **216**, 1487–1496 (2019).

54. K. Basso, R. Dalla-Favera, Germinal centres and B cell lymphomagenesis. *Nat. Rev. Immunol.* **15**, 172–184 (2015).

55. J. A. Healy, A. Nugent, R. E. Rempel, A. B. Moffitt, N. S. Davis, X. Jiang, J. R. Shingleton, J. Zhang, C. Love, J. Datta, M. E. McKinney, T. J. Tzeng, N. Wettschureck, S. Offermanns, K. A. Walzer, J. T. Chi, S. A. K. Rasheed, P. J. Casey, I. S. Lossos, S. S. Dave, GNA13 loss

in germinal center B cells leads to impaired apoptosis and promotes lymphoma in vivo. *Blood* **127**, 2723–2731 (2016).

56. R. Schmitz, G. W. Wright, D. W. Huang, C. A. Johnson, J. D. Phelan, J. Q. Wang, S. Roulland, M. Kasbekar, R. M. Young, A. L. Shaffer, D. J. Hodson, W. Xiao, X. Yu, Y. Yang, H. Zhao, W. Xu, X. Liu, B. Zhou, W. du, W. C. Chan, E. S. Jaffe, R. D. Gascoyne, J. M. Connors, E. Campo, A. Lopez-Guillermo, A. Rosenwald, G. Ott, J. Delabie, L. M. Rimsza, K. Tay Kuang Wei, A. D. Zelenetz, J. P. Leonard, N. L. Bartlett, B. Tran, J. Shetty, Y. Zhao, D. R. Soppet, S. Pittaluga, W. H. Wilson, L. M. Staudt, Genetics and pathogenesis of diffuse large B-cell lymphoma. *N. Engl. J. Med.* **378**, 1396–1407 (2018).

57. B. Chapuy, C. Stewart, A. J. Dunford, J. Kim, A. Kamburov, R. A. Redd, M. S. Lawrence, M. G. M. Roemer, A. J. Li, M. Ziepert, A. M. Staiger, J. A. Wala, M. D. Ducar, I. Leshchiner, E. Rheinbay, A. Taylor-Weiner, C. A. Coughlin, J. M. Hess, C. S. Pedamallu, D. Livitz, D. Rosebrock, M. Rosenberg, A. A. Tracy, H. Horn, P. van Hummelen, A. L. Feldman, B. K. Link, A. J. Novak, J. R. Cerhan, T. M. Habermann, R. Siebert, A. Rosenwald, A. R. Thorner, M. L. Meyerson, T. R. Golub, R. Beroukhim, G. G. Wulf, G. Ott, S. J. Rodig, S. Monti, D. S. Neuberg, M. Loeffler, M. Pfreundschuh, L. Trümper, G. Getz, M. A. Shipp, Molecular subtypes of diffuse large B cell lymphoma are associated with distinct pathogenic mechanisms and outcomes. *Nat. Med.* **24**, 679–690 (2018).

58. C. Sha, S. Barrans, F. Cucco, M. A. Bentley, M. A. Care, T. Cummin, H. Kennedy, J. S. Thompson, R. Uddin, L. Worrillow, R. Chalkley, M. van Hoppe, S. Ahmed, T. Maishman, J. Caddy, A. Schuh, C. Mamot, C. Burton, R. Tooze, A. Davies, M. Q. du, P. W. M. Johnson, D. R. Westhead, Molecular high-grade B-cell lymphoma: Defining a poor-risk group that requires different approaches to therapy. *J. Clin. Oncol.* **37**, 202–212 (2019).

59. X. Ye, W. Ren, D. Liu, X. Li, W. Li, X. Wang, F. L. Meng, L. S. Yeap, Y. Hou, S. Zhu, R. Casellas, H. Zhang, K. Wu, Q. Pan-Hammarström, Genome-wide mutational signatures revealed distinct developmental paths for human B cell lymphomas. *J. Exp. Med.* **218**, e20200573 (2021).

60. N. J. Ingham, F. Carlisle, S. Pearson, M. A. Lewis, A. Buniello, J. Chen, R. L. Isaacson, J. Pass, J. K. White, S. J. Dawson, K. P. Steel, S1PR2 variants associated with auditory function in humans and endochlear potential decline in mouse. *Sci. Rep.* **6**, 28964 (2016).

61. Y. P. Wu, K. Mizugishi, M. Bektas, R. Sandhoff, R. L. Proia, Sphingosine kinase 1/S1P receptor signaling axis controls glial proliferation in mice with Sandhoff disease. *Hum. Mol. Genet.* **17**, 2257–2264 (2008).

62. L. Cruz-Orengo, B. P. Daniels, D. Dorsey, S. A. Basak, J. G. Grajales-Reyes, E. E. McCandless, L. Piccio, R. E. Schmidt, A. H. Cross, S. D. Crosby, R. S. Klein, Enhanced sphingosine-1-phosphate receptor 2 expression underlies female CNS autoimmunity susceptibility. *J. Clin. Invest.* **124**, 2571–2584 (2014).

63. A. Skoura, T. Sanchez, K. Claffey, S. M. Mandala, R. L. Proia, T. Hla, Essential role of sphingosine 1-phosphate receptor 2 in pathological angiogenesis of the mouse retina. *J. Clin. Invest.* **117**, 2506–2516 (2007).

64. T. Sanchez, A. Skoura, M. T. Wu, B. Casserly, E. O. Harrington, T. Hla, Induction of vascular permeability by the sphingosine-1-phosphate receptor-2 (S1P2R) and its downstream effectors ROCK and PTEN. *Arterioscler. Thromb. Vasc. Biol.* **27**, 1312–1318 (2007).

65. A. Skoura, J. Michaud, D. S. Im, S. Thangada, Y. Xiong, J. D. Smith, T. Hla, Sphingosine-1-phosphate receptor-2 function in myeloid cells regulates vascular inflammation and atherosclerosis. *Arterioscler. Thromb. Vasc. Biol.* **31**, 81–85 (2011).

66. J. Michaud, D. S. Im, T. Hla, Inhibitory role of sphingosine 1-phosphate receptor 2 in macrophage recruitment during inflammation. *J. Immunol.* **184**, 1475–1483 (2010).

67. H. Ikeda, N. Watanabe, I. Ishii, T. Shimosawa, Y. Kume, T. Tomiya, Y. Inoue, T. Nishikawa, N. Ohtomo, Y. Tanoue, S. Iitsuka, R. Fujita, M. Omata, J. Chun, Y. Yatomi, Sphingosine 1-phosphate regulates regeneration and fibrosis after liver injury via sphingosine 1-phosphate receptor 2. *J. Lipid Res.* **50**, 556–564 (2009).

68. J. Zhao, Y. Okamoto, Y. Asano, K. Ishimaru, S. Aki, K. Yoshioka, N. Takuwa, T. Wada, Y. Inagaki, C. Takahashi, T. Nishiuchi, Y. Takuwa, Sphingosine-1-phosphate receptor-2 facilitates pulmonary fibrosis through potentiating IL-13 pathway in macrophages. *PLOS ONE* **13**, e0197604 (2018).

69. R. O. Dror, T. J. Mildorf, D. Hilger, A. Manglik, D. W. Borhani, D. H. Arlow, A. Philippsen, N. Villanueva, Z. Yang, M. T. Lerch, W. L. Hubbell, B. K. Kobilka, R. K. Sunahara, D. E. Shaw, Structural basis for nucleotide exchange in heterotrimeric G proteins. *Science* **348**, 1361–1365 (2015).

70. S. Q. Zheng, E. Palovcak, J. P. Armache, K. A. Verba, Y. Cheng, D. A. Agard, MotionCor2: Anisotropic correction of beam-induced motion for improved cryo-electron microscopy. *Nat. Methods* **14**, 331–332 (2017).

71. A. Rohou, N. Grigorieff, CTFFIND4: Fast and accurate defocus estimation from electron micrographs. *J. Struct. Biol.* **192**, 216–221 (2015).

72. S. H. W. Scheres, RELION: Implementation of a Bayesian approach to cryo-EM structure determination. *J. Struct. Biol.* **180**, 519–530 (2012).

73. A. Punjani, J. L. Rubinstein, D. J. Fleet, M. A. Brubaker, cryoSPARC: Algorithms for rapid unsupervised cryo-EM structure determination. *Nat. Methods* **14**, 290–296 (2017).

74. K. Krishna Kumar, M. Shalev-Benami, M. J. Robertson, H. Hu, S. D. Banister, S. A. Hollingsworth, N. R. Latorraca, H. E. Kato, D. Hilger, S. Maeda, W. I. Weis, D. L. Farrens, R. O. Dror, S. V. Malhotra, B. K. Kobilka, G. Skiniotis, Structure of a signaling cannabinoid receptor 1-G protein complex. *Cell* **176**, 448–458.e12 (2019).

75. E. F. Pettersen, T. D. Goddard, C. C. Huang, G. S. Couch, D. M. Greenblatt, E. C. Meng, T. E. Ferrin, UCSF Chimera—A visualization system for exploratory research and analysis. *J. Comput. Chem.* **25**, 1605–1612 (2004).

76. P. Emsley, K. Cowtan, Coot: Model-building tools for molecular graphics. *Acta Crystallogr. D Biol. Crystallogr.* **60**, 2126–2132 (2004).

77. P. D. Adams, P. V. Afonine, G. Bunkóczi, V. B. Chen, I. W. Davis, N. Echols, J. J. Headd, L.-W. Hung, G. J. Kapral, R. W. Grosse-Kunstleve, A. J. M. Coy, N. W. Moriarty, R. Oeffner, R. J. Read, D. C. Richardson, J. S. Richardson, T. C. Terwilliger, P. H. Zwart, PHENIX: A comprehensive Python-based system for macromolecular structure solution. *Acta Crystallogr. D Biol. Crystallogr.* **66**, 213–221 (2010).

78. V. B. Chen, W. B. Arendall III, J. J. Headd, D. A. Keedy, R. M. Immormino, G. J. Kapral, L. W. Murray, J. S. Richardson, D. C. Richardson, MolProbity: All-atom structure validation for macromolecular crystallography. *Acta Crystallogr. D Biol. Crystallogr.* **66**, 12–21 (2010).

79. D. Devost, R. Sleno, D. Pétrin, A. Zhang, Y. Shinjo, R. Okde, A. Inoue, T. E. Hébert, Conformational profiling of the AT1 angiotensin II receptor reflects biased agonism, G protein coupling, and cellular context. *J. Biol. Chem.* **292**, 5443–5456 (2017).

80. E. Lu, F. D. Wolfreys, J. R. Muppidi, Y. Xu, J. G. Cyster, S-Geranylgeranyl-L-glutathione is a ligand for human B cell-confinement receptor P2RY8. *Nature* **567**, 244–248 (2019).